Enhanced passivity of Cr-Fe-Co-Ni-Mo multi-component single-phase face-centred cubic alloys: design, production and corrosion behaviour

Xueying Wang, Dimitri Mercier, Yolaine Danard, Thomas Rieger, Loïc Perrière, Mathilde Laurent-Brocq, Ivan Guillot, Vincent Maurice, Philippe Marcus

To cite this version:

Xueying Wang, Dimitri Mercier, Yolaine Danard, Thomas Rieger, Loïc Perrière, et al.. Enhanced passivity of Cr-Fe-Co-Ni-Mo multi-component single-phase face-centred cubic alloys: design, production and corrosion behaviour. Corrosion Science, 2022, 200, pp.110233. ⟨10.1016/j.corsci.2022.110233⟩. ⟨hal-03607706⟩

HAL Id: hal-03607706
https://hal.science/hal-03607706v1

Submitted on 14 Mar 2022

Author preprint published in *Corrosion Science*
https://doi.org/10.1016/j.corsci.2022.110233

Enhanced passivity of Cr-Fe-Co-Ni-Mo multi-component single-phase face-centred cubic alloys: design, production and corrosion behaviour

Xueying WANG[1], Dimitri MERCIER[1*], Yolaine DANARD[2], Thomas RIEGER[2], Loïc PERRIERE[2], Mathilde LAURENT-BROCQ[2*], Ivan GUILLOT[2], Vincent MAURICE[1], Philippe MARCUS[1*]

[1] *PSL Research University, CNRS - Chimie ParisTech, Institut de Recherche de Chimie Paris, Physical Chemistry of Surfaces Group,* 11 rue Pierre et Marie Curie, *75005 Paris, France*

[2] *Université Paris Est Creteil, CNRS, ICMPE, UMR7182, Thiais F-94320, France*

**Corresponding authors: D. Mercier (dimitri.mercier@chimieparistech.psl.eu), M. LAURENT-BROCQ (laurent-brocq@icmpe.cnrs.fr), P. Marcus (philippe.marcus@chimieparistech.psl.eu).*

Abstract

The vast composition space of the Cr-Fe-Co-Ni-Mo system was explored by massive thermodynamic calculations in order to design and characterize multi-component single-phase *fcc* alloys optimized in Cr and Mo content and having enhanced passivity. Adding up to 15 at.% Mo while retaining the *fcc* single-phase is possible, which is unprecedented. Cr is confirmed to be a prerequisite to ensure self-protection against corrosion by passivation. Adding Mo up to 10 at.% tremendously enhances the resistance to passivity breakdown in Cl^--containing aggressive environment. Newly designed quinary alloys, $Cr_{25}Fe_{25}Co_5Ni_{40}Mo_5$ and $Cr_{15}Fe_{10}Co_5Ni_{60}Mo_{10}$ (at.%), show superior resistance to localized corrosion.

Keywords

Multi-principal element alloys; passivity; pitting corrosion; thermodynamic diagrams; production; microstructure

1 Introduction

Multi-principal element alloys (MPEA), also named high entropy alloys (HEA) or multi-component alloys, are alloys forming a solid-solution in which all components are very concentrated. The concept emerged following the discovery of an equimolar CrMnFeCoNi alloy unexpectedly found to be single-phase [1,2]. Some of these alloys have a face-centred cubic (*fcc*) crystalline structure when based on transition metals, like the CrMnFeCoNi Cantor alloy [3], while others are body-centred cubic (*bcc*) when based on refractory metals [4,5]. Equimolar quinary alloys were primarily studied because of their very good mechanical properties [6,7], like in the case of the Cantor alloy that exhibits an excellent combination of strength and ductility [8,9]. Another advantage of multi-component alloys is their wide and unexplored composition space. Indeed, systematic thermodynamic calculations have identified many compositions that are single-phase [10,11]. Effort focused on improving solid solution strengthening (SSS) has revealed that many single-phase compositions have higher SSS than the equimolar Cantor alloy [12–14]. This wide composition space can also be explored to optimize other properties, such as corrosion resistance of Cr-containing alloys such as stainless steels or stainless alloys that are of tremendous importance for many industrial applications and in everyday life.

The well-known promoting impact of Cr alloying on corrosion performance is due to the formation of a protective oxide layer, the passive film, nanometer-thick and enriched in Cr(III) (hydr)oxide as already widely reported for stainless steels for instance [15–23]. Likewise, recent studies on Cr-containing multi-component alloys confirmed their passivation behaviour and showed that the quaternary CoCrFeNi system, for example, is even more resistant than some traditional stainless steels [24,25]. However, the quinary CoCrFeMnNi Cantor alloy, although containing 20 at.% Cr, does not show good corrosion resistance, especially in chloride-containing solutions [26,27]. Some studies suggested that this degradation of the corrosion resistance is due to the detrimental effect of Mn addition on the stability of the passive film that provides the corrosion protection [26–28]. In contrast, Mo alloying element is well-known to be beneficial to the corrosion resistance when no σ-phase is formed, especially in more aggressive Cl^--containing environment [29–37], which has been recently confirmed for as-cast FeCoCrNiMo HEA [38,39]. Two mechanisms are still debated to explain this beneficial effect of Mo. The first one is based on the stratified structure of the oxide film with Mo oxides concentrated in the exchange outer layer and Cr oxide in the barrier inner layer [40,41]. On as-cast FeCoCrNiMo HEA, the addition of Mo would decrease the point defect density in the passive film [38]. Mo would impede the penetration of Cl^- ions into the oxide film, thus mitigating passivity breakdown [32,35]. The other mechanism proposes that metallic Mo would promote self-repairing of the passive film in the defect sites locally exposed to the environment after passivity breakdown [37,42].

Here, we report on the design and selection, production, and microstructure and corrosion resistance characterization of multi-component single-phase *fcc* alloys containing Cr and Mo, the two key elements for achieving stable passivity. Cr and Mo contents were studied to question whether the deleterious effect of Mn on the corrosion performance of the Cantor alloy can be counteracted by substitution with Mo. Modelling and experimental approaches were combined. The resistance to passivity breakdown and the initiation to localized corrosion in Cl^--containing solution was compared to those of the Cantor alloy, a stainless steel grade (SS 316L) and a Ni-based stainless alloy (Ni23Cr6Mo) also containing Cr and Mo. The results show how insightful this combined approach is to make benefit of the wide compositional space offered by the quinary Cr-Fe-Co-Ni-Mo system in order to combine the beneficial effects of Cr and Mo for promoting the passivity of multi-component single-phase fcc alloys and achieving superior corrosion resistance.

2 Methods

2.1 Modelling and simulation methods

Modelling was performed using the CALPHAD approach to calculate the phase diagram of the quinary Cr-Fe-Co-Ni-Mo system. The CALPHAD method relies on a self-consistent description of Gibbs energy for each phase of a system. Semi-empirical functions are used that depend on temperature and composition, and are optimized based on experimental phase diagrams, thermodynamic data and *ab-initio* results. Once a database consisting of semi-empirical equations and the corresponding fitting parameters has been developed, it can be used to calculate phase diagrams [43].

Thermo-Calc now includes new databases dedicated to HEA [13]. In principle, these databases can be used for any composition and they were already proven to reproduce experimental results for various systems [10,11,44]. In TCHEA3 database, which was the most recent at the moment of the study, 8 ternary sub-systems from the Cr-Fe-Co-Ni-Mo system were assessed, compared to only 6 in TCHEA1. Thus, TCHEA3 should be more reliable and was the database selected for this study. The Co-Cr-Mo sub-system, which is of interest in this study, was assessed in TCHEA1 and not in TCHEA3. The present work confirms the reliability of TCHEA3.

An isopleth was calculated and plotted. The principle is to vary the atomic composition of one element, here Mo, while retaining the content of other elements in equimolar proportion, which can be written as: $Cr_{\frac{1-x}{4}}Fe_{\frac{1-x}{4}}Co_{\frac{1-x}{4}}Ni_{\frac{1-x}{4}}Mo_{x}$. This approach enables us to determine the Mo solubility in the *fcc* phase for the quaternary Cr-Fe-Co-Ni system. The whole quinary Cr-Fe-Co-Ni-Mo phase diagram was then simulated. To do so, the stable phases were calculated at 1273 K, by varying the composition of each element stepwise in 5 at.% increments. This represents more than 10 000 compositions, including 3 876 quinaries, 4 845 quaternaries, 1 710 ternaries and 190 binaries.

2.2 Sample production and characterisation methods

Four compositions were selected and prepared with the same procedure. Cr, Fe, Co, Ni and Mo metals, with a purity exceeding 99.9 wt %, were melted by high frequency induction under a He atmosphere into an ingot of around 60 g. Gravity casting was used to shape the ingots into a rod with a diameter of 13 mm and a length of around 60 mm. The as-cast rods were machined so as to have two planes parallel to the casting direction and a thickness of 9 mm. Cold-rolling was performed with a thickness reduction of 89 % to obtain a sheet with a thickness of 1 mm. The sheets were punched to disks of 15 mm in diameter. The last step was homogenisation and recrystallization annealing under a He atmosphere. Samples were wrapped into a tantalum sheet, introduced into the hot furnace at 1100°C, annealed and quickly cooled down while still in the He atmosphere. The duration of the annealing varied between 1 to 3 h, depending on the samples. More details on the choice of the duration are given in Section 3.2.

All samples in the as-cast and annealed states were characterised by scanning electronmMicroscopy (SEM) equipped with a back-scattered electron (BSE) detector and coupled with an energy dispersive X-ray spectrometer (EDS). The average composition of each sample was measured with low magnification (× 300) EDS mapping. Higher magnification (× 1500) mapping was also performed to check that alloys were single-phased. SEM-BSE images were used to determine the average grain size using the lineal intercept method [45]. The reported uncertainty is the 95 % confidence interval.

All samples in the annealed state were also characterized by X-ray diffraction (XRD) using a PANAlytical X'Pert Pro diffractometer and the Co-Kα radiation at a wavelength of 0.178897 nm. For each pattern, the four diffracting peaks were fitted by a pseudo-Voigt function. The lattice parameter of the *fcc* phase was calculated using the Bragg formula. The reported values and uncertainties correspond to the average and standard deviation over the four peaks, respectively.

The hardness of each sample in the annealed state was measured using a FM-700 Vickers micro-indenter at a 200 gf load. The given hardness and uncertainty are the average and standard deviation over 15 measurements, respectively.

2.3 Electrochemical methods

For electrochemical analysis, the surfaces were mechanically polished to a mirror finish with SiC paper of 1200, 2400 and 4000 grades followed by diamond polishing with 3, 1 and 0.25 µm suspensions. After polishing, samples were cleaned in ultrasonic baths of acetone, ethanol and deionized water (Merk Millipore, resistivity of 18.2 MΩ.cm), and dried in a flow of compressed air.

Electrochemical measurements were performed using a VersaSTAT4 potentiostat (AMETEK) in a 3-electrode cell comprising a saturated mercury sulphate reference electrode (MSE, $E_{SHE} = E_{MSE} + 0.64$ V), a Pt wire as counter electrode and the alloy sample as working electrode. The working electrode area, delimited by a Viton O-ring, is estimated to be 1.13 cm^2. Electrochemical measurements were carried out at room temperature in 0.05 M H_2SO_4 electrolyte without or with NaCl, prepared from ultrapure chemicals (VWR) and deionized water. Before each experiment, solutions were deaerated by Ar bubbling for 30 min to minimize dissolved gas.

Before each electrochemical polarization, the open circuit potential was recorded for 15 min, after which the potential was stable. Potentiodynamic polarizations were performed by linear scan voltammetry from -1.21 V to 0.8 V/MSE at a scanning rate of 1 mV/s. Chronoamperometric measurements were performed at 0 V/MSE in two steps during which the current transient was measured. The potential of 0 V/MSE was imposed during 1 h in Cl^--free 0.05 M H_2SO_4 in order to passivate the sample in the absence of chlorides. Then at the same potential, chloride ions (NaCl) were added to the electrolyte every 10 minutes to reach a concentration of 1, 2, 3 ,4, 4.3, 4.5 and 4.7 M while keeping the concentration of H_2SO_4 at 0.05 M.

3 Results and discussion

3.1 Thermodynamic modelling and composition selection

Figure 1 shows the $(CrFeCoNi)_{100-x}Mo_x$ isopleth calculated using the CALPHAD method in order to estimate the maximum Mo content that can be added to the quaternary Cr-Fe-Co-Ni system while keeping it single-phase *fcc*. The single-phase *fcc* domain of interest is restricted to the range of high temperature and low Mo content. For many high entropy alloys, like the CrFeCoMnNi Cantor alloy [46], the *fcc* phase is the high temperature stable state but it can be easily retained at room temperature. Here, for the quaternary CrFeCoNi alloy, the *fcc* phase is stable down to around 900 K, and the lower limit of the *fcc* domain, i.e. the transus temperature, increases when adding Mo. In other words, the *fcc* domain shrinks and ends at around

4 at.% Mo. Afterwards, a sigma phase precipitates in addition to the *fcc* phase. Due to the elevated transus temperature, it would not be possible to retain the *fcc* phase bearing 4 at.% Mo at room temperature. In this work, we considered that the transus temperature should have a maximum value of 1000°C (or 1273 K) for a possible quenching of the *fcc* phase down to room temperature. At this temperature, the maximum content in the *fcc* phase is around 1 at.% Mo (as marked by red double headed arrow and dashed line in Figure 1). In experimental studies, alloys referred to as $CrFeCoNiMo_{0.1}$ (2.4 at.% Mo) [38] and $CrFeCoNiMo_{0.2}$ (4.8 at.% Mo) [47] were found to be single-phase *fcc* while an alloy referred to as $CrFeCoNiMo_{0.3}$ (7 at.% Mo) [38,47] contained a sigma phase. Our thermodynamic calculations are in qualitative agreement with these results although these alloys were studied as-cast and thus not representative of the stable state. Adding Mo is therefore detrimental to the stability of the *fcc* phase, an effect also known for Cr [11,48]. Thus, maximizing the content of both Cr and Mo while remaining single-phase *fcc* is challenging and requires a systematic exploration of possible compositions.

The complete quinary diagram shown in Figure 2 was calculated for a temperature of 1273 K. It is presented using a matrix of quasi-ternary FeCoNi phase diagrams with the Cr and Mo concentrations increasing along the horizontal and vertical axes, respectively. In each quasi-ternary FeCoNi diagram, the Cr and Mo contents are fixed. The quasi-ternary diagrams with Cr and Mo contents higher than 45 and 20 at.%, respectively, are not plotted since they do not contain any *fcc* phase (marked in red). This quinary diagram confirms the well-known effect of Cr and Mo in destabilizing, e.g., the single-phase *fcc* structure of iron-based alloys. On the top line, upon increasing the Cr content, the single-phase *fcc* composition decreases. The same trend is observed along the left column when increasing the Mo content. The quinary representation also shows that the destabilizing role of Cr is drastically promoted when adding Mo. Indeed, with 10 at.% Mo for example, the maximum content for retaining some *fcc* phase is 20 at.% Cr whereas it is 45 at.% Cr without Mo.

Based on this quinary diagram, four compositional areas of interest marked A, B, C and D in Figure 2 were selected for alloy synthesis. Areas A and B were chosen in order to maximize the content of either Mo or Cr, respectively, so as to independently study their role in determining the corrosion properties, while areas C and D were selected in order to maximize simultaneously the Mo and Cr contents. In order to choose one composition per area of interest, two additional criteria were added: (i) [Fe] and [Co] $\neq 0$ so as to produce multi-component alloys and (ii) [Fe] > [Co] because Fe is much less expensive than Co and Ni (the other replacement alternative). The four selected compositions are listed in Table 1. Up to 10 and 15 at.% of Mo were added in the quinary (MPEA-15Cr-10Mo) alloy and quaternary (MPEA-15Mo) alloys, respectively. This is largely higher than the maximum Mo content experimentally reported [47] or predicted on the CrFeCoNi-Mo isopleth (Figure 1).

Finally, the evolution of the phase fraction with temperature was calculated with the CALPHAD method for all the selected compositions (Figure S1 in supplementary information) and the transus temperature was determined (Table 1). For all samples, the difference between the solidus and the transus temperatures seems large enough to perform a high temperature homogenisation annealing and then to cool down the alloy while maintaining the high temperature stable state.

3.2 Production and microstructure

The four alloys listed in Table 1 were prepared by induction melting of pure metals and casting, as commonly done for MPEA [3,6,49] although powder metallurgy is also emerging [50,51]. The as-cast microstructures were found to be dendritic as shown in Figure S2 in Supplementary information, with more or less pronounced Mo segregation. It was checked that, within the detection limit of XRD and SEM-EDS, those microstructures did not contain any secondary phases, which could be hard and/or fragile and compromise cold-rolling. After cold-rolling, homogenisation and recrystallization were combined in a single annealing treatment. A temperature of 1100°C was chosen, which is higher by at least 120°C than the transus temperature (Table 1), in order to avoid precipitation during cooling of the secondary phases predicted by the thermodynamic calculations (Figure S1). The microsegregation model proposed by Kattamis *et al.* [52] was used to calculate the annealing duration required to homogenise the dendritic structure. The characteristic dimension of the dendritic structure was measured on SEM images and the diffusion coefficients were taken from Tsai *et al.* [53] for Cr, Fe, Co and Ni and from Nitta *et al.* for Mo [54]. A minimum duration of 30 min was calculated. The second objective of the annealing treatment was to recrystallize and grow grains larger than 50 µm so as to minimize the effect of grain boundaries on corrosion properties and allow us to focus on the influence of the *fcc* phase composition. Different durations were tested, with 30 minutes as a starting point. The selected durations were 3 h for MPEA-15Mo and MPEA-15Cr10Mo, 1 h for MPEA-35Cr and 2 h for MPEA-25Cr5Mo.

The microstructural characterization of the MPEA-15Cr10Mo sample in the final state (i.e. after annealing under the selected conditions) is observed in Figure 3. The results are similar for the other three alloys (Figures S3 to S5 in supplementary information). It shows that the recrystallization was achieved, resulting in grains with a regular shape and an average size of 61 µm (Figure 3a, Table 1). The dendritic microstructure was fully homogenised, resulting in a random distribution of the elements (Figure 3b). No secondary phase was detected on EDS mapping. On the XRD pattern, the four peaks are indexed as belonging to the *fcc* phase and no other peak is observed, confirming that there is no secondary phase. Thus, as desired, the four selected alloys are composed of a single-phase *fcc* solid solution. Those results are in very good agreement with the CALPHAD thermodynamic calculations and indicate that the TCHEA3 database is reliable, at least for the studied range of composition. It is to be mentioned that 1 to 3 h annealing at 1100°C may not be sufficient to reach the stable thermodynamic state. This could be checked by longer annealing in the future.

From XRD measurements, the *fcc* lattice parameter was determined and it varies depending on the composition (Table 1). When comparing the MPEA-35Cr and MPEA-15Mo alloys, it seems that the lattice parameter increases with the content of Mo. But this trend is not confirmed when comparing the MPEA-25Cr5Mo and MPEA-15Cr10Mo alloys. As already observed in the Co-Cr-Fe-Mn-Ni system [12], the evolution of the lattice parameter with composition is complex in this multi-component system. The microhardness was also measured. It varies from 148 ± 5 HV for MPEA-35Cr up to 200 ± 10 HV for MPEA-15Cr10Mo. So, increasing the Mo content seems to increase the hardness. This is consistent with the observed increase of the lattice parameter. However, the MPEA-15Mo and MPEA-15Cr10Mo samples exhibit the same hardness although their Mo content differs by 5 at.%. As for the lattice parameter and as already observed in the Co-Cr-Fe-Mn-Ni system [12], the evolution with composition of the solid solution strengthening and, consequently, of the hardness is not straightforward in multi-component alloys.

3.3 Passivity and resistance to Cl^--induced localized corrosion

Figure 4a shows the polarization curves recorded in the Cl^--free 0.05 M H_2SO_4 solution for the four processed alloys. The curve obtained for the Cantor alloy is also shown for comparison. The values of the corrosion potential, compiled in Table 2, are close. All alloys present a similar passivation behavior, except for MPEA-15Mo. In the anodic region, the active domain is observed between -0.71 and -0.55V and characterized by a passivation peak. The value of the current density at the passivation peak depends on the composition of the alloy (Table 2). The Cantor alloy shows the highest current density at the passivation peak, suggesting that, before anodic passivation, the native oxide present at the surface limits active dissolution than on the other alloys less effectively. For the four Cr-containing alloys, the passive domain spreads from -0.55 to 0.45V with a minimum of current density reached at a potential close to 0 V/MSE. This value is similar to that observed on 316L stainless steel [23] and will be selected for formation of the passive films by anodic potentiostatic polarization. For the quaternary alloy without Cr (MPEA-15Mo), the passive region is quite narrow with the current density increasing quite steeply right after the active/passive transition, indicating no stable formation of a protective passive oxide film. For all other alloys having increasingly higher chromium content (MPEA-15Cr10Mo, MPEA-25Cr5Mo and MPEA-35Cr), current densities at the active/passive transition and in the passive domain are lower and decrease with increasing Cr content (Table 2), demonstrating the beneficial role of chromium on the corrosion protection provided by the native and passive oxide layers.

Figure 4b, 4c and 4d present the polarization curves obtained for MPEA-35Cr, MPEA-15Cr10Mo and MPEA-25Cr5Mo, respectively, in 0.05 M H_2SO_4 solution of different NaCl concentrations. For the MPEA-35Cr sample, a slight cathodic shift (-60mV) of the corrosion potential is observed in the presence of chloride (Table 2). In the anodic domain, the current density measured during the active/passive transition increases strongly with increasing NaCl concentration, showing that the protection properties of the native oxide layer decrease and the presence of chlorides poisons the formation of the passive film. At the NaCl concentration of 5 M, the absence of an extended passive domain indicates that the chloride ions impede the formation of a stable passive layer.

For the MPEA-15Cr10Mo (Figure 4c) and MPEA-25Cr5Mo (Figure 4d) alloys, the passivation behaviour is very similar with or without chlorides in the electrolyte. The current densities at the active/passive transition, as well as in the passive domain, remain unchanged for increasing NaCl concentrations (Table 2). This indicates that the pre-formed native oxide films and the anodically formed passive oxide films all resist the deleterious effect of Cl^- on the corrosion resistance. Noticeably, the fact that Cl^- does not reduce the width of the passive domain nor increase the passive current density shows the high stability of the protection provided by the passive films on these Mo-containing multi-component alloys. Similar results were obtained in Cl^--containing 0.5 M H_2SO_4 solutions with alloys referred to as $CrFeCoNiMo_{0.1}$ (2.4 at.% Mo), $CrFeCoNiMo_{0.3}$ (7 at.% Mo) and $CrFeCoNiMo_{0.6}$ as-cast alloys [38] among which only the $CrFeCoNiMo_{0.1}$ (2.4 at.% Mo) alloy was found to be single-phase fcc [39]. Our results, obtained with stabilized single-phase *fcc* alloys, show that the promoting effect of Mo addition on passivity can be sustained for a lower Cr content of 15 at%.

Figure 5 presents the time evolution of the passivation current density recorded during anodic polarization at 0 V/MSE for the MPEA-15Cr10Mo (Figure 5a), MPEA-25Cr5Mo (Figure 5b) and MPEA-35Cr (Figure 5c) alloys in 0.05 M H_2SO_4 electrolyte. After 1 h of polarization, NaCl was added so as to increase every 10 min the chloride ion concentration to the specified values. For better visibility, the first 3 000 seconds of passivation in the absence of chlorides are not shown in Figure 5, but presented separately in Figure 6. Similar curves obtained for SS 316L (Figure 5e), Ni23Cr6Mo (Figure 5d) and Cantor alloy (Figure 5f) are also presented for comparison.

During anodic passivation in the Cl^--free solution (Figure 6), all six alloys show a similar and classical evolution of the current density, characterized first by a strong (about 3 orders of magnitude) and fast decrease owing to formation of the passive film, and followed by a longer time of stabilization where surfaces slowly evolve towards the steady state of passivity. For all alloys, lower current densities than at OCP are reached showing enhanced protection properties of the passive film compared to the native oxide film. Comparing the MPEA-15Cr10Mo, MPEA-25Cr5Mo and MPEA-35Cr alloys, one notices that the current density reached after 3 000 seconds of polarization decreases with increasing Cr content of the alloy, confirming the effect of this element on the barrier properties of the passive film.

During the second step of the experiment during which Cl^- ions are added (Figure 5), the passive current density evolves differently depending on the alloy, evidencing the differences of resistance to passivity breakdown and initiation of localized corrosion between the tested alloys. For the MPEA-15Cr10Mo and MPEA-25Cr5Mo samples that contain both Cr and Mo, the current density remains low and even keeps decreasing after the addition of chlorides into the electrolyte. A high Cl^- concentration (4.7 M) does not lead to any electrochemical noise with current spikes above background that would be characteristic of passivity breakdown and metastable pitting. This shows that these two alloys have excellent corrosion resistance with no effect of the presence of chlorides on the steady state of passivity.

For the quaternary alloy containing only Cr (MPEA-35Cr), the current density before exposure to chlorides is initially lower than for the two quinary alloys (49 nA/cm^2 compared to 316 nA/cm^2 and 152 nA/cm^2 for MPEA-15Cr10Mo and MPEA-25Cr5Mo, respectively), indicating a more protective steady state of passivity in Cl^--free electrolyte. However, the addition of chloride induces spikes of current density already at 2 M concentration, indicative of passivity breakdown followed by repair (metastable pitting), and a steep increase of the current density at 3 M concentration, indicative of the initiation of stable pitting after breakdown of the passive film.

For comparison, the behaviour of the Cantor alloy (considered as the reference alloy for the HEA *fcc* structure), 316L stainless steel and a NiCrMo stainless alloy is also shown in Figure 5. Already at low chloride concentration, the Cantor alloy exhibits passivity alteration (0.3 M) and passivity breakdown followed by the initiation of stable pitting (0.4 M). This difference confirms that, in the absence of Mo alloying to substitute Mn, the passive film is not stable in chloride-containing environment despite the Cr content of 20 at.% Cr of the bulk alloy. Substituting Mn by Mo in the quinary MPEAs has the expected beneficial effect on the corrosion properties with formation of a passive film resistant to degradation in the presence of chlorides.

For 316L stainless steel, the current spikes indicative of passivity breakdown and repair appear at 1 M Cl^- concentration. This is followed by the initiation of stable pitting at 3 M Cl^- concentration in the tested conditions. For the Ni-based (NiCrMo) stainless alloy, no spike or steep increase of the current density is observed after adding chlorides, indicating the absence of initiation of localized corrosion, particularly by pitting corrosion. However, the gradual increase of the current density (from 120 nA/cm^2 before adding chlorides to 600 nA/cm^2 at 4.7 M Cl^-) shows the degradation of the steady state of passivity although without real breakdown of the passive layer. We interpret this behaviour as due to faster dissolution in the passive state, but with simultaneous reformation of the passive film.

The current transients shown in Figure 5 and obtained at 0 V in chloride-containing solution after anodic formation of the passive film in the absence of chlorides clearly show the beneficial effect of combined alloying of Cr and Mo on corrosion resistance of multi-component *fcc* systems, with Cr providing protection against generalized corrosion and Mo combatting both local passivity breakdown and the initiation of pitting corrosion. Comparing the polarization curves of MPEA-15Mo to those of MPEA-35Cr, MPEA-15Cr10Mo and MPEA-25Cr5Mo in Figure 4, it is comfirmed that the addition of Cr in these MPEAs is crucial to form a protective and stable passive film on their surface, as proved for many Cr-containing traditional alloys [15–20,22,23]. Comparing the four Cr-containing alloys in Figure 4a, the passive current densities show a negative correlation with Cr content in alloy, while the ending potential of the passive domain shows a positive correlation. However, the protecting effect of the passive film formed when Cr is alloyed without Mo is limited in sulfuric acid at high Cl^- concentration, as shown by the local breakdown of the passive film and initiation of stable pitting observed for MPEA-35Cr at 3 M Cl^- in Figure 5d. The difference between Figure 4b where the passive domain is still measurable in 3 M Cl^- at the scan rate of 1 mV/s and Figure 5d where the passive film breaks down at 0 V and 3 M Cl^- may come from the induction period before pitting corrosion initiation [55–58], as suggested in Figure 5d where the breakdown of the passive film appears only after 5 min of polarisation. The addition of molybdenum in these Cr-containing *fcc* MPEAs strongly increases the corrosion resistance of these materials (Figure 5a, 5b and 5c), confirming the beneficial role of Mo, known for conventional alloys [15,30,31] and recently demonstrated for as-cast multi-component alloys [39]. Especially, the substitution of Mn by Mo improves the corrosion resistance in Cl^--containing sulfuric acid solution enormously. It is interesting to note that the two quinary alloys, newly-designed, with stabilized single-phase *fcc*, are not only far more resistant than the Cantor alloy and traditional SS 316L, but also more resistant than Ni23Cr6Mo, in which the content on Cr and Mo is similar to

MPEA-25Cr5Mo. Further insight from surface analysis of the enhanced passivity of these single-phase *fcc* MPEAs will be reported separately.

4 Conclusion

The massive thermodynamic calculations applied in this work to the Cr-Fe-Co-Ni-Mo multi-component system using the CALPHAD method show that, despite the destabilizing effect of Cr and Mo, quaternary and quinary alloys of maximized content in these two elements can remain single-phase *fcc.* Based on systematic calculations of the quinary phase diagram, four multi-component alloys of selected maximized Cr and Mo contents were processed and the microstructural characterization showed that they were single-phased *fcc* in agreement with the thermodynamic predictions. Our results show that it is possible to add up to 15 at.% Mo, while retaining the *fcc* single-phase, which is an unprecedented result.

Electrochemical behavior and corrosion performance of the processed alloys were investigated in sulfuric acid with various Cl^- concentrations. Alloying of Cr is confimed to be a prerequisite to ensure self-protection against corrosion by passive film formation. Adding Mo tremendously enhances the resistance to passivity breakdown in Cl^--containing aggressive environment. The two newly designed quinary alloys, $Cr_{25}Fe_{25}Co_5Ni_{40}Mo_5$ and $Cr_{15}Fe_{10}Co_5Ni_{60}Mo_{10}$ (at.%), show a resistance to localized corrosion in Cl^--containing solution far superior to that of Fe-based and Ni-based traditional alloys containing Cr and Mo.

This work has shown that chromium and molybdenum, key elements for enhanced corrosion resistance, can be alloyed with higher contents in single-phase multi component alloys, while keeping the desired *fcc* single phase structure. In this way, alloys with extremely high corrosion resistance are obtained.

Acknowledgments

The authors are grateful to Elie Protopopoff for preliminary thermodynamic calculations. This work was supported by the European Research Council (ERC) under the European Union’s Horizon 2020 research and innovation programme (ERC Advanced Grant agreement No 741123).

References

[1] B. Cantor, I.T.H. Chang, P. Knight, A.J.B. Vincent, Microstructural development in equiatomic multicomponent alloys, Materials Science and Engineering: A. 375–377 (2004) 213–218. https://doi.org/10.1016/j.msea.2003.10.257.

[2] J.-W. Yeh, S.-K. Chen, S.-J. Lin, J.-Y. Gan, T.-S. Chin, T.-T. Shun, C.-H. Tsau, S.-Y. Chang, Nanostructured High-Entropy Alloys with Multiple Principal Elements: Novel Alloy Design Concepts and Outcomes, Advanced Engineering Materials. 6 (2004) 299–303. https://doi.org/10.1002/adem.200300567.

[3] M. Laurent-Brocq, A. Akhatova, L. Perrière, S. Chebini, X. Sauvage, E. Leroy, Y. Champion, Insights into the phase diagram of the CrMnFeCoNi high entropy alloy, Acta Materialia. 88 (2015) 355–365. https://doi.org/10.1016/j.actamat.2015.01.068.

[4] J.P. Couzinié, G. Dirras, L. Perrière, T. Chauveau, E. Leroy, Y. Champion, I. Guillot, Microstructure of a near-equimolar refractory high-entropy alloy, Materials Letters. 126 (2014) 285–287. https://doi.org/10.1016/j.matlet.2014.04.062.

[5] O.N. Senkov, D.B. Miracle, K.J. Chaput, J.-P. Couzinie, Development and exploration of refractory high entropy alloys—A review, Journal of Materials Research. 33 (2018) 3092–3128. https://doi.org/10.1557/jmr.2018.153.

[6] D.B. Miracle, O.N. Senkov, A critical review of high entropy alloys and related concepts, Acta Materialia. 122 (2017) 448–511. https://doi.org/10.1016/j.actamat.2016.08.081.

[7] E.J. Pickering, N.G. Jones, High-entropy alloys: a critical assessment of their

founding principles and future prospects, International Materials Reviews. 61 (2016) 183–202. https://doi.org/10.1080/09506608.2016.1180020.

[8] B. Gludovatz, A. Hohenwarter, D. Catoor, E.H. Chang, E.P. George, R.O. Ritchie, A fracture-resistant high-entropy alloy for cryogenic applications, Science. 345 (2014) 1153–1158. https://doi.org/10.1126/science.1254581.

[9] G. Laplanche, A. Kostka, O.M. Horst, G. Eggeler, E.P. George, Microstructure evolution and critical stress for twinning in the CrMnFeCoNi high-entropy alloy, Acta Materialia. 118 (2016) 152–163. https://doi.org/10.1016/j.actamat.2016.07.038.

[10] O.N. Senkov, J.D. Miller, D.B. Miracle, C. Woodward, Accelerated exploration of multi-principal element alloys with solid solution phases, Nat Commun. 6 (2015) 6529. https://doi.org/10.1038/ncomms7529.

[11] G. Bracq, M. Laurent-Brocq, L. Perrière, R. Pirès, J.-M. Joubert, I. Guillot, The fcc solid solution stability in the Co-Cr-Fe-Mn-Ni multi-component system, Acta Materialia. 128 (2017) 327–336. https://doi.org/10.1016/j.actamat.2017.02.017.

[12] G. Bracq, M. Laurent-Brocq, C. Varvenne, L. Perrière, W.A. Curtin, J.-M. Joubert, I. Guillot, Combining experiments and modeling to explore the solid solution strengthening of high and medium entropy alloys, Acta Materialia. 177 (2019) 266–279. https://doi.org/10.1016/j.actamat.2019.06.050.

[13] F.G. Coury, K.D. Clarke, C.S. Kiminami, M.J. Kaufman, A.J. Clarke, High Throughput Discovery and Design of Strong Multicomponent Metallic Solid Solutions, Sci Rep. 8 (2018) 8600. https://doi.org/10.1038/s41598-018-26830-6.

[14] F. Tancret, I. Toda-Caraballo, E. Menou, P.E.J. Rivera Díaz-Del-Castillo, Designing high entropy alloys employing thermodynamics and Gaussian process statistical analysis, Materials & Design. 115 (2017) 486–497. https://doi.org/10.1016/j.matdes.2016.11.049.

[15] I. Olefjord, The passive state of stainless steels, Materials Science and Engineering. 42 (1980) 161–171. https://doi.org/10.1016/0025-5416(80)90025-7.

[16] A.R. Brooks, C.R. Clayton, K. Doss, Y.C. Lu, On the Role of Cr in the Passivity of Stainless Steel, J. Electrochem. Soc. 133 (1986) 2459–2464.

[17] P. Marcus, J.M. Grimal, The anodic dissolution and passivation of NiCrFe alloys studied by ESCA, Corrosion Science. 33 (1992) 805–814. https://doi.org/10.1016/0010-938X(92)90113-H.

[18] P. Marcus, On some fundamental factors in the effect of alloying elements on passivation of alloys, Corrosion Science. 36 (1994) 2155–2158. https://doi.org/10.1016/0010-938X(94)90013-2.

[19] V. Maurice, W.P. Yang, P. Marcus, X-Ray Photoelectron Spectroscopy and Scanning Tunneling Microscopy Study of Passive Films Formed on (100) Fe—i 8Cr—i 3Ni Single-Crystal Surfaces, (n.d.) 12.

[20] E. Gardin, S. Zanna, A. Seyeux, A. Allion-Maurer, P. Marcus, Comparative study of the surface oxide films on lean duplex and corresponding single phase stainless steels by XPS and ToF-SIMS, Corrosion Science. 143 (2018) 403–413.

https://doi.org/10.1016/j.corsci.2018.08.009.

[21] V. Maurice, P. Marcus, Progress in corrosion science at atomic and nanometric scales, Progress in Materials Science. 95 (2018) 132–171. https://doi.org/10.1016/j.pmatsci.2018.03.001.

[22] E. Gardin, S. Zanna, A. Seyeux, A. Allion-Maurer, P. Marcus, XPS and ToF-SIMS characterization of the surface oxides on lean duplex stainless steel – Global and local approaches, Corrosion Science. 155 (2019) 121–133. https://doi.org/10.1016/j.corsci.2019.04.039.

[23] Z. Wang, E.-M. Paschalidou, A. Seyeux, S. Zanna, V. Maurice, P. Marcus, Mechanisms of Cr and Mo Enrichments in the Passive Oxide Film on 316L Austenitic Stainless Steel, Front. Mater. 6 (2019) 232. https://doi.org/10.3389/fmats.2019.00232.

[24] Y. Qiu, S. Thomas, M.A. Gibson, H.L. Fraser, N. Birbilis, Corrosion of high entropy alloys, Npj Mater Degrad. 1 (2017) 15. https://doi.org/10.1038/s41529-017-0009-y.

[25] P. Muangtong, A. Rodchanarowan, D. Chaysuwan, N. Chanlek, R. Goodall, The corrosion behaviour of CoCrFeNi-x (x = Cu, Al, Sn) high entropy alloy systems in chloride solution, Corrosion Science. (2020) 108740. https://doi.org/10.1016/j.corsci.2020.108740.

[26] L. Wang, D. Mercier, S. Zanna, A. Seyeux, M. Laurent-Brocq, L. Perriere, I. Guillot, P. Marcus, Study of the surface oxides and corrosion behaviour of an equiatomic CoCrFeMnNi high entropy alloy by XPS and ToF-SIMS, Corrosion Science. (2020) 108507. https://doi.org/10.1016/j.corsci.2020.108507.

[27] J. Yang, J. Wu, C.Y. Zhang, S.D. Zhang, B.J. Yang, W. Emori, J.Q. Wang, Effects of Mn on the electrochemical corrosion and passivation behavior of CoFeNiMnCr high-entropy alloy system in H2SO4 solution, Journal of Alloys and Compounds. 819 (2020) 152943. https://doi.org/10.1016/j.jallcom.2019.152943.

[28] S. Fajardo, I. Llorente, J.A. Jiménez, J.M. Bastidas, D.M. Bastidas, Effect of Mn additions on the corrosion behaviour of TWIP Fe-Mn-Al-Si austenitic steel in chloride solution, Corrosion Science. 154 (2019) 246–253. https://doi.org/10.1016/j.corsci.2019.04.026.

[29] A. Elbiache, P. Marcus, The role of molybdenum in the dissolution and the passivation of stainless steels with adsorbed sulphur, Corrosion Science. 33 (1992) 261–269. https://doi.org/10.1016/0010-938X(92)90150-2.

[30] K. Sugimoto, Y. Sawada, The role of molybdenum additions to austenitic stainless steels in the inhibition of pitting in acid chloride solutions, Corrosion Science. 17 (1977) 425–445. https://doi.org/10.1016/0010-938X(77)90032-4.

[31] G.O. Ilevbare, G.T. Burstein, The role of alloyed molybdenum in the inhibition of pitting corrosion in stainless steels, Corrosion Science. (2001) 29.

[32] T. Yamamoto, K. Fushimi, M. Seo, S. Tsuri, T. Adachi, H. Habazaki, Depassivation–repassivation behavior of type-312L stainless steel in NaCl solution investigated by the micro-indentation, Corrosion Science. 51 (2009)

1545–1553. https://doi.org/10.1016/j.corsci.2008.11.020.

[33] X.-L. Shang, Z.-J. Wang, Q.-F. Wu, J.-C. Wang, J.-J. Li, J.-K. Yu, Effect of Mo Addition on Corrosion Behavior of High-Entropy Alloys CoCrFeNiMox in Aqueous Environments, Acta Metall. Sin. (Engl. Lett.). 32 (2019) 41–51. https://doi.org/10.1007/s40195-018-0812-7.

[34] W. Wang, J. Wang, H. Yi, W. Qi, Q. Peng, Effect of Molybdenum Additives on Corrosion Behavior of (CoCrFeNi)(100-x)Mo-x High-Entropy Alloys, Entropy. 20 (2018) 908. https://doi.org/10.3390/e20120908.

[35] A.A. Rodriguez, J.H. Tylczak, M.C. Gao, P.D. Jablonski, M. Detrois, M. Ziomek-Moroz, J.A. Hawk, Effect of Molybdenum on the Corrosion Behavior of High-Entropy Alloys CoCrFeNi$_2$ and CoCrFeNi$_2$Mo$_{0.25}$ under Sodium Chloride Aqueous Conditions, Advances in Materials Science and Engineering. 2018 (2018) 1–11. https://doi.org/10.1155/2018/3016304.

[36] Z. Niu, Y. Wang, C. Geng, J. Xu, Y. Wang, Microstructural evolution, mechanical and corrosion behaviors of as-annealed CoCrFeNiMo (x = 0, 0.2, 0.5, 0.8, 1) high entropy alloys, Journal of Alloys and Compounds. 820 (2020) 153273. https://doi.org/10.1016/j.jallcom.2019.153273.

[37] J.D. Henderson, X. Li, D.W. Shoesmith, J.J. Noël, K. Ogle, Molybdenum surface enrichment and release during transpassive dissolution of Ni-based alloys, Corrosion Science. 147 (2019) 32–40. https://doi.org/10.1016/j.corsci.2018.11.005.

[38] C. Dai, H. Luo, J. Li, C. Du, Z. Liu, J. Yao, X-ray photoelectron spectroscopy and electrochemical investigation of the passive behavior of high-entropy FeCoCrNiMox alloys in sulfuric acid, Applied Surface Science. 499 (2020) 143903. https://doi.org/10.1016/j.apsusc.2019.143903.

[39] C. Dai, T. Zhao, C. Du, Z. Liu, D. Zhang, Effect of molybdenum content on the microstructure and corrosion behavior of FeCoCrNiMox high-entropy alloys, Journal of Materials Science & Technology. 46 (2020) 64–73. https://doi.org/10.1016/j.jmst.2019.10.020.

[40] V. Maurice, H. Peng, L.H. Klein, A. Seyeux, S. Zanna, P. Marcus, Effects of molybdenum on the composition and nanoscale morphology of passivated austenitic stainless steel surfaces, Faraday Discuss. 180 (2015) 151–170. https://doi.org/10.1039/C4FD00231H.

[41] E. De Vito, P. Marcus, XPS study of passive films formed on molybdenum-implanted austenitic stainless steels, Surf. Interface Anal. 19 (1992) 403–408. https://doi.org/10.1002/sia.740190175.

[42] R.C. Newman, The dissolution and passivation kinetics of stainless alloys containing molybdenum—1. Coulometric studies of Fe□Cr and Fe□Cr□Mo alloys, Corrosion Science. 25 (1985) 331–339. https://doi.org/10.1016/0010-938X(85)90111-8.

[43] M. Perrut, Thermodynamic modeling by the calphad method and its applications to innovative materials, Aerospace Lab. (2015) 1–11.

[44] T. Rieger, J.-M. Joubert, M. Laurent-Brocq, L. Perrière, I. Guillot, J.-P. Couzinié,

Study of the FCC+L12 two-phase region in complex concentrated alloys based on the Al–Co–Cr–Fe–Ni–Ti system, Materialia. 14 (2020) 100905. https://doi.org/10.1016/j.mtla.2020.100905.

[45] E04 Committee, Standard test Methods for Determining Average Grain Size, ASTM International, n.d. https://doi.org/10.1520/E0112-10.

[46] F. Otto, A. Dlouhý, K.G. Pradeep, M. Kuběnová, D. Raabe, G. Eggeler, E.P. George, Decomposition of the single-phase high-entropy alloy CrMnFeCoNi after prolonged anneals at intermediate temperatures, Acta Materialia. 112 (2016) 40–52. https://doi.org/10.1016/j.actamat.2016.04.005.

[47] W.H. Liu, Z.P. Lu, J.Y. He, J.H. Luan, Z.J. Wang, B. Liu, Y. Liu, M.W. Chen, C.T. Liu, Ductile CoCrFeNiMox high entropy alloys strengthened by hard intermetallic phases, Acta Materialia. 116 (2016) 332–342. https://doi.org/10.1016/j.actamat.2016.06.063.

[48] G. Laplanche, S. Berglund, C. Reinhart, A. Kostka, F. Fox, E.P. George, Phase stability and kinetics of σ-phase precipitation in CrMnFeCoNi high-entropy alloys, Acta Materialia. 161 (2018) 338–351. https://doi.org/10.1016/j.actamat.2018.09.040.

[49] L. Lilensten, J.-P. Couzinié, L. Perrière, A. Hocini, C. Keller, G. Dirras, I. Guillot, Study of a bcc multi-principal element alloy: Tensile and simple shear properties and underlying deformation mechanisms, Acta Materialia. 142 (2018) 131–141. https://doi.org/10.1016/j.actamat.2017.09.062.

[50] X. Ni, T. Dai, T. Lu, J. Pan, M. Li, J. Dai, Microstructure and properties of CrMnFeCoNi high-entropy alloy prepared by mechanical alloying and spark plasma sintering, Powder Metallurgy. 62 (2019) 38–43. https://doi.org/10.1080/00325899.2018.1554834.

[51] M. Laurent-Brocq, D. Mereib, G. Garcin, J. Monnier, L. Perrière, B. Villeroy, Chemical architecturation of high entropy alloys through powder metallurgy, Journal of Alloys and Compounds. 835 (2020) 155279. https://doi.org/10.1016/j.jallcom.2020.155279.

[52] T. Kattamis, M. Flemings, Dendrite Morphology Microsegregation and Homogenization of Low-Alloy Steel, Transactions of the Metallurgical Society of Aime. 233 (1965) 992-.

[53] K.-Y. Tsai, M.-H. Tsai, J.-W. Yeh, Sluggish diffusion in Co–Cr–Fe–Mn–Ni high-entropy alloys, Acta Materialia. 61 (2013) 4887–4897. https://doi.org/10.1016/j.actamat.2013.04.058.

[54] H. Nitta, T. Yamamoto, R. Kanno, K. Takasawa, T. Iida, Y. Yamazaki, S. Ogu, Y. Iijima, Diffusion of molybdenum in α-iron, Acta Materialia. 50 (2002) 4117–4125. https://doi.org/10.1016/S1359-6454(02)00229-X.

[55] M. Janik- Czachor, An Assessment of the Processes Leading to Pit Nucleation on Iron, J. Electrochem. Soc. 128 (1981) 513C-519C. https://doi.org/10.1149/1.2127344.

[56] M. Urquidi, D.D. Macdonald, Solute- Vacancy Interaction Model and the Effect of Minor Alloying Elements on the Initiation of Pitting Corrosion, J.

Electrochem. Soc. 132 (1985) 555–558. https://doi.org/10.1149/1.2113886.

[57] G.T. Burstein, P.C. Pistorius, S.P. Mattin, The nucleation and growth of corrosion pits on stainless steel, Corrosion Science. 35 (1993) 57–62. https://doi.org/10.1016/0010-938X(93)90133-2.

[58] P. Guo, E.C. La Plante, B. Wang, X. Chen, M. Balonis, M. Bauchy, G. Sant, Direct observation of pitting corrosion evolutions on carbon steel surfaces at the nano-to-micro- scales, Sci Rep. 8 (2018) 7990. https://doi.org/10.1038/s41598-018-26340-5.

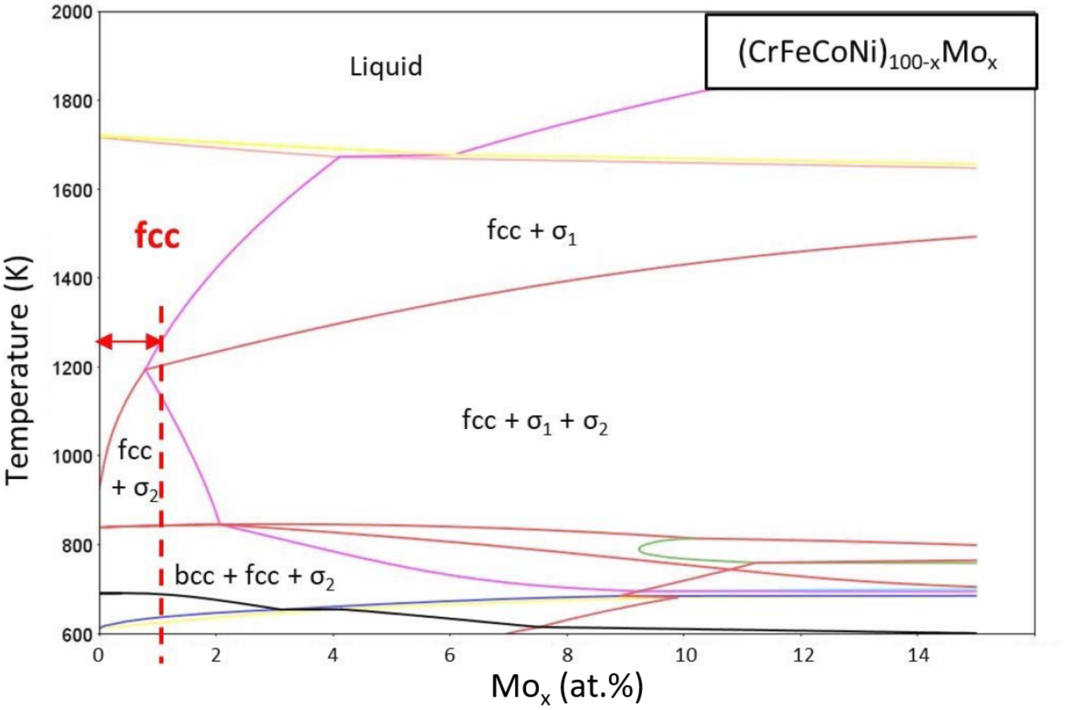

Figure 1 Isopleth section calculated with the CALPHAD method and the TCHEA3 database for (CrFeCoNi)$_{100-x}$Mo$_x$. The red double headed arrow and dashed line indicate the Mo concentration to obtain a *fcc* single-phase alloy at 1273 K.

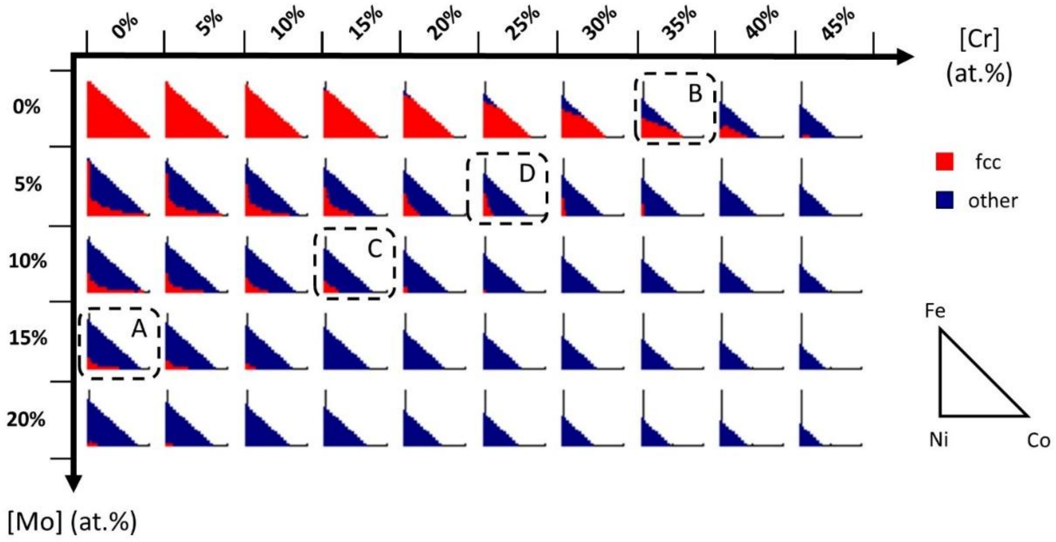

Figure 2 Matrix representation of a section of the quinary Cr-Fe-Co-Ni-Mo phase diagram calculated at 1273 K with the CALPHAD method and the TCHEA3 database. One quasi-ternary FeCoNi diagram is schemed on the right. A red square indicates a single *fcc* solid solution whereas a blue square indicates other cases (several phases). The processed compositions were selected within the dashed rectangles labelled A to D.

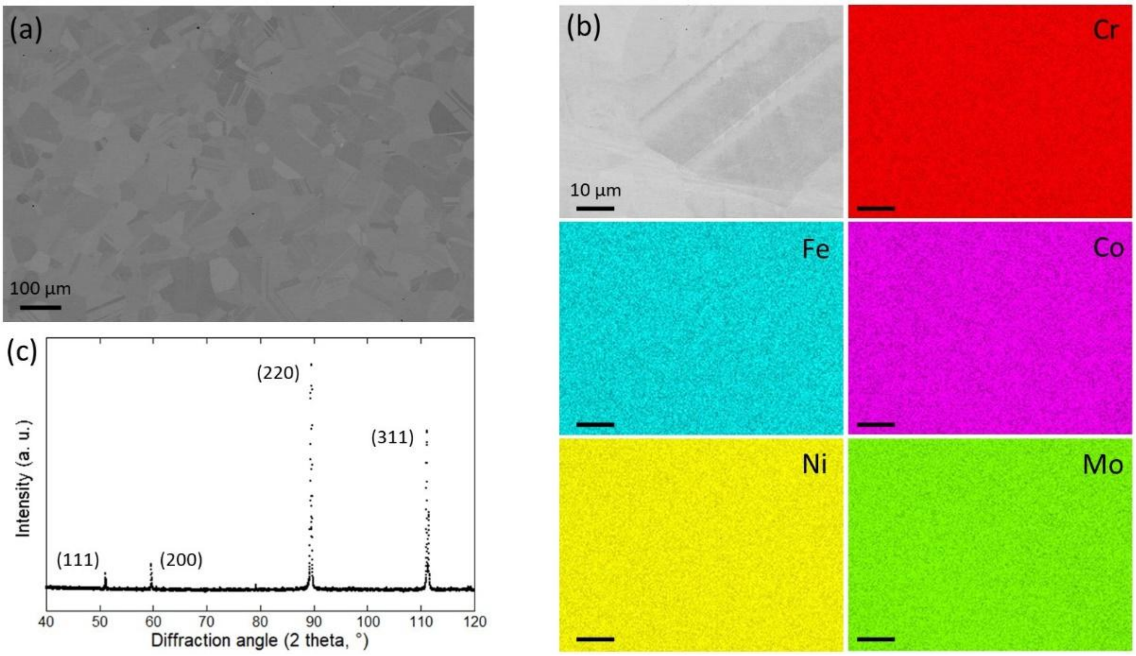

Figure 3 Microstructural characterization of the annealed MPEA-15Cr10Mo alloy. (a) SEM-BSE image, (b) SEM-BSE image and EDS mapping and (c) XRD.

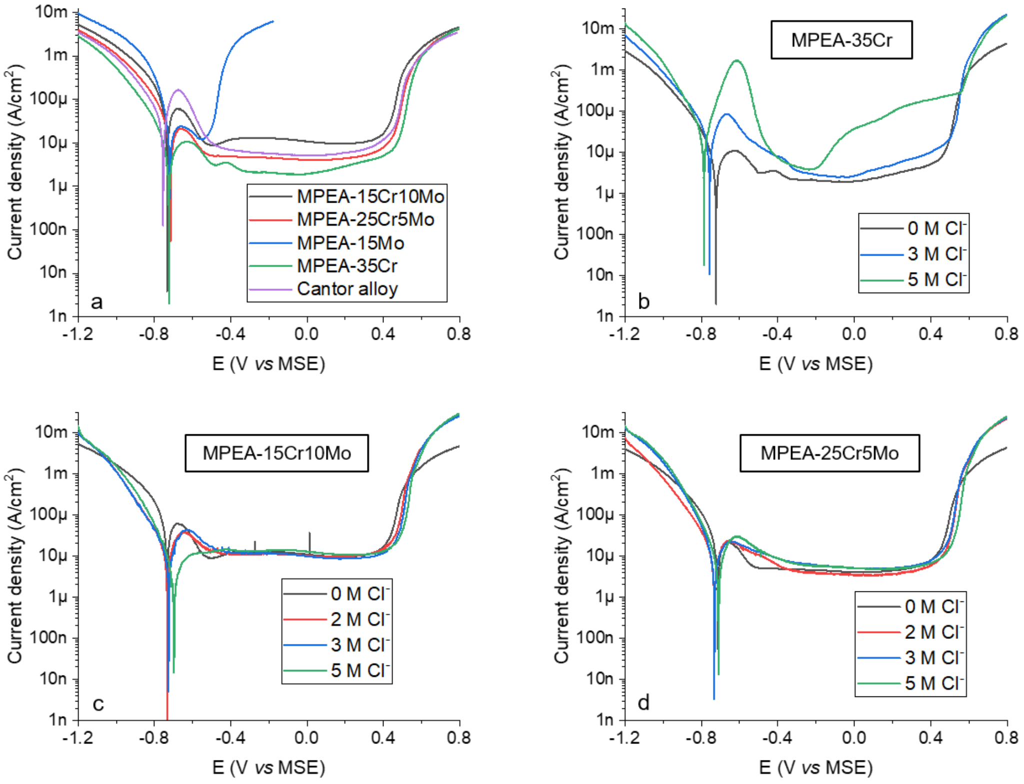

Figure 4 Potentiodynamic analysis of the passivation behaviour for the MPEA systems: (a) MPEA-15Cr10Mo, MPEA-25Cr5Mo, MPEA-15Mo, MPEA-35Cr and Cantor alloy in Cl$^-$-free 0.05 M H_2SO_4. (b) MPEA-35Cr in 0.05 M H_2SO_4 with 0, 3 and 5 M NaCl. (c) MPEA-15Cr10Mo in 0.05 M H_2SO_4 with 0, 2, 3 and 5 M NaCl. (d) MPEA-25Cr5Mo in 0.05 M H_2SO_4 with 0, 2, 3 and 5 M NaCl. Scanning rate is 1mV/s.

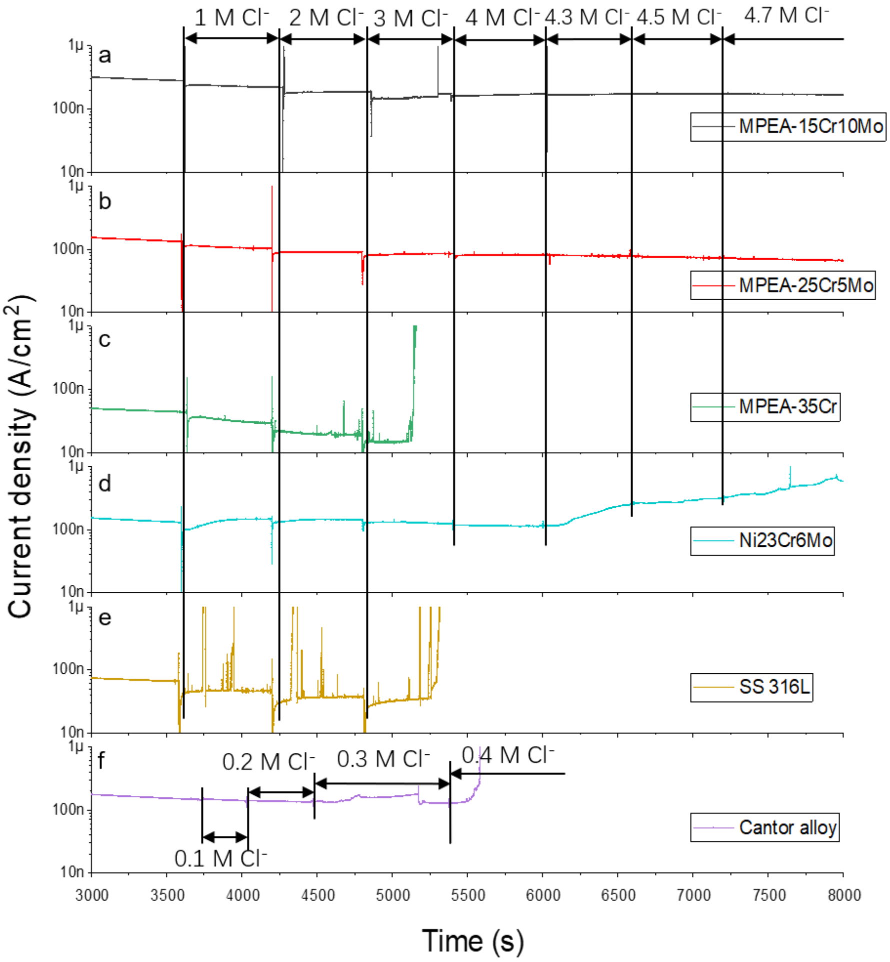

Figure 5 Potentiostatic analysis of passivity breakdown and initiation of localized corrosion at 0 V/MSE in 0.05 M H_2SO_4 with increasing Cl^- concentration as marked: (a) MPEA-15Cr10Mo, (b) MPEA-25Cr5Mo, (c) MPEA-35Cr, (d) Ni23Cr6Mo, (e) 316L SS, (f) Cantor alloy. Chlorides are added after 3 600 s of passivation in Cl^--free 0.05 M H_2SO_4.

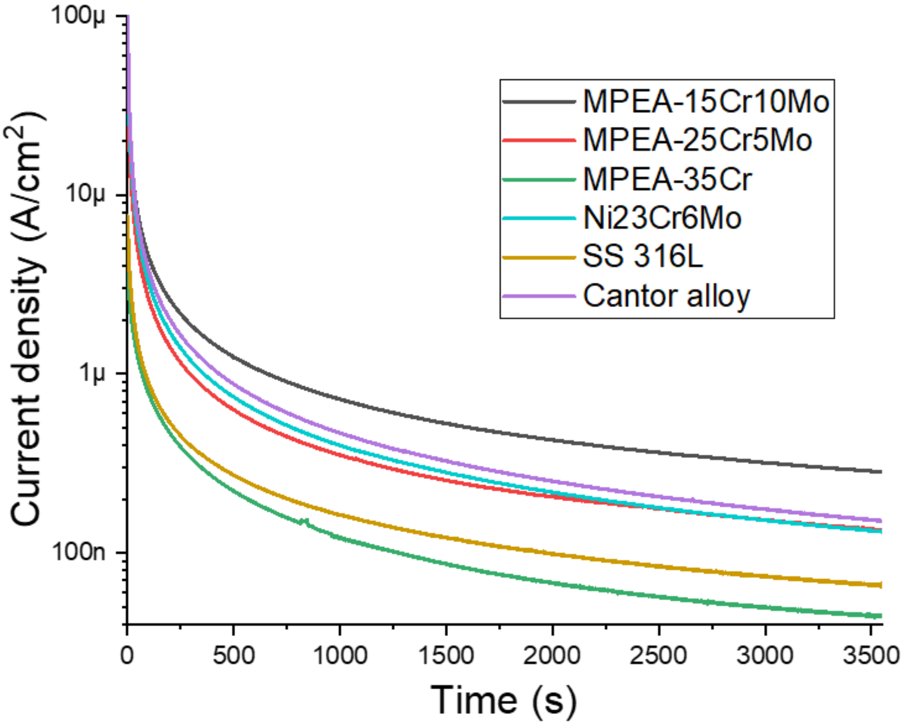

Figure 6 Potentiostatic passivation at 0 V/MSE in Cl$^-$-free 0.05 M H_2SO_4. Current variation is presented from 0 to 3 600 s of polarization for MPEA-15Cr10Mo, MPEA-25Cr5Mo, MPEA-35Cr, Ni23Cr6Mo, 316L SS, and Cantor alloy.

Table 1 List of the processed samples. The transus temperature was calculated by the CALPHAD method (with TC-HEA3 database). The composition, the grain size, the lattice parameter and the hardness were measured by SEM-EDS, EBSD, XRD and micro-indentation, respectively.

Sample	Nominal concentration (at.%)	Transus temperature (°C)	Annealing temperature (°C)	Measured composition (at.%)	Grain diameter (µm)	Lattice parameter (Å)	Hardness (HV)
MPEA-25Cr5Mo	$Cr_{25}Fe_{25}Co_5Ni_{40}Mo_5$	980	1100	$Cr_{25}Fe_{25}Co_5Ni_{38.8}Mo_{5.2}$	66 ± 3	3.5980	175 ± 5
MPEA-15Cr10Mo	$Cr_{15}Fe_{10}Co_5Ni_{60}Mo_{10}$	945	1100	$Cr_{15}Fe_{10}Co_5Ni_{59}Mo_{10}$	61 ± 5	3.5972	200 ± 10
MPEA-35Cr	$Cr_{35}Fe_{20}Co_5Ni_{40}$	865	1100	$Cr_{35}Fe_{20}Co_5Ni_{38.9}$	69 ± 5	3.579 (4)	148 ± 5
MPEA-15Mo	$Fe_{10}Co_5Ni_{70}Mo_{15}$	910	1100	$Fe_{10}Co_5Ni_{69.7}Mo_{14.6}$	60 ± 8	3.6003	199 ± 8

Table 2 Corrosion potential, maximum active current density and minimum passive current density of MPEA15Cr10Mo, MPEA25Cr5Mo, MPEA15Mo, MPEA35Cr and Cantor alloy in 0.05 M H_2SO_4 for increasing concentration of Cl^-.

Alloy	NaCl concentration (M)	Corrosion potential E_{corr} (mV)	Maximum active current density (μA/cm^2)	Minimum passive current density (μA/cm^2)
MPEA-15Cr10Mo	0	-728 ± 5	60.8	9.6
	2	-727 ± 3	37.8	9.3
	3	-725 ± 6	42.6	8.5
	5	-700 ± 10	11.9	10.6
MPEA-25Cr5Mo	0	-718 ± 4	21.2	4.0
	2	-732 ± 2	22.9	3.3
	3	-731 ± 6	22.3	4.9
	5	-710 ± 5	29.9	4.7
MPEA-15Mo	0	-717 ± 8	23.9	-
MPEA-35Cr	0	-716 ± 7	10.6	1.9
	3	-765 ± 9	84.0	2.5
	5	-785 ± 6	1670.0	3.8
Cantor alloy	0	-760 ± 10	165.0	5.1

Supplementary information for:

Enhanced passivity of Cr-Fe-Co-Ni-Mo multi-component single-phase face-centred cubic alloys: design, production and corrosion behaviour

Xueying WANG[1], Dimitri MERCIER[1*], Yolaine DANARD[2], Thomas RIEGER[2], Loïc PERRIERE[2], Mathilde LAURENT-BROCQ[2*], Ivan GUILLOT[2], Vincent MAURICE[1], Philippe MARCUS[1*]

[1] *PSL Research University, CNRS - Chimie ParisTech, Institut de Recherche de Chimie Paris, Physical Chemistry of Surfaces Group,* 11 rue Pierre et Marie Curie, *75005 Paris, France*

[2] *Université Paris Est Creteil, CNRS, ICMPE, UMR7182, Thiais F-94320, France*

**Corresponding authors: D. Mercier (dimitri.mercier@chimieparistech.psl.eu), M. LAURENT-BROCQ (laurent-brocq@icmpe.cnrs.fr), P. Marcus (philippe.marcus@chimieparistech.psl.eu).*

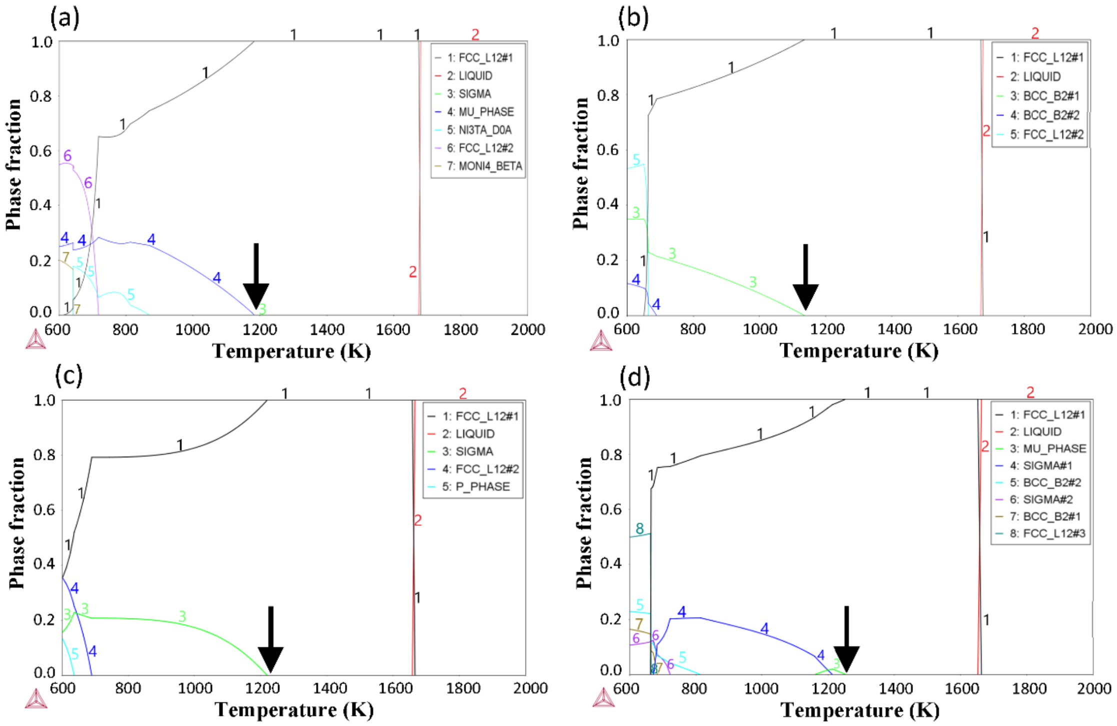

Figure S1 Evolution with temperature of the phase fraction calculated with the CALPHAD method and the TCHEA3 database for (a) MPEA-15Mo, (b) MPEA-35Cr, (c) MPEA-15Cr10Mo and (d) MPEA-25Cr5Mo. The black arrows indicate the transus temperature (i.e. the formation of a second phase).

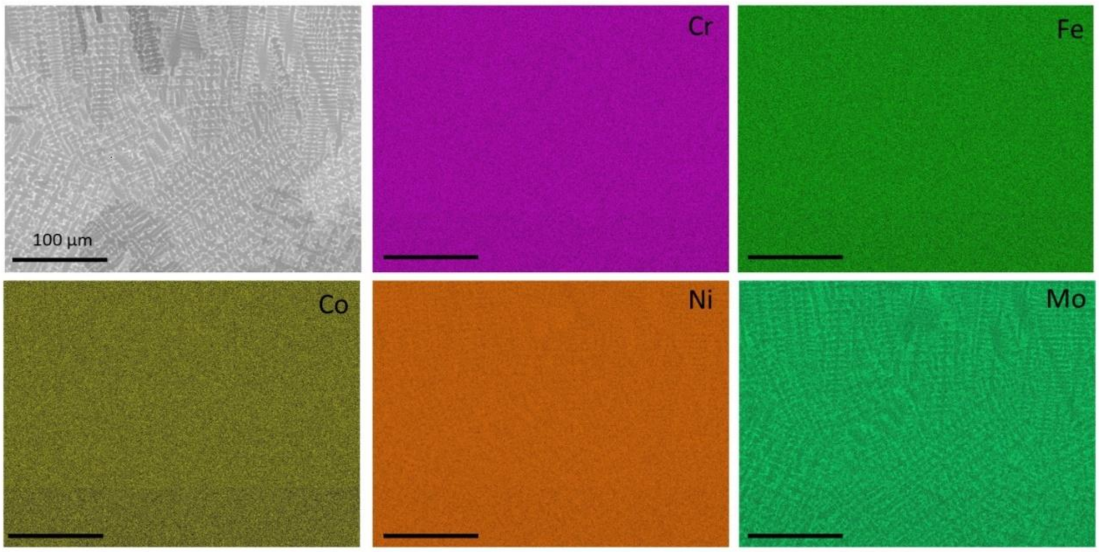

Figure S2 SEM-BSE image and EDS mapping of the as-cast MPEA-15Cr10Mo alloy.

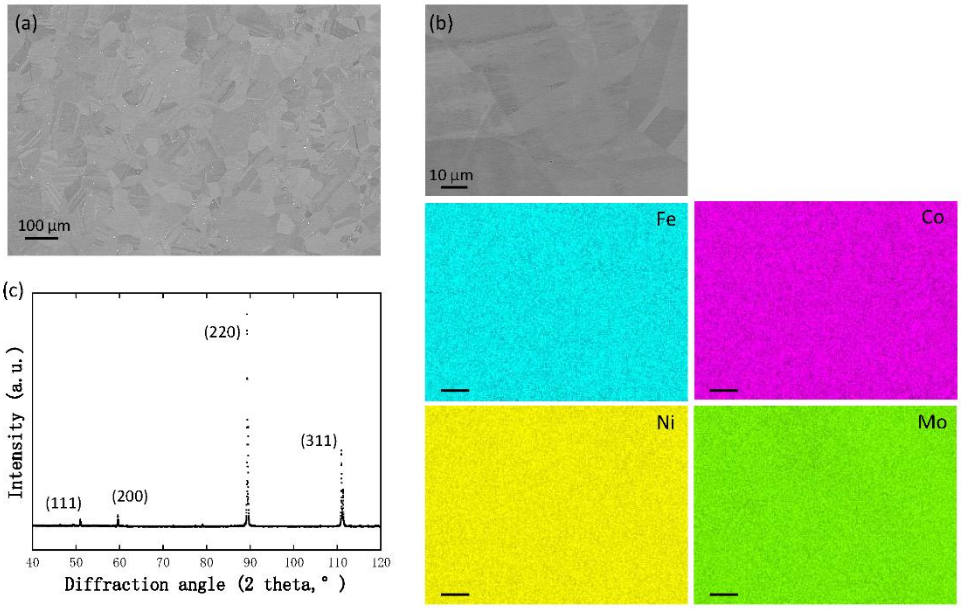

Figure S3 Microstructural characterization of the annealed MPEA-15Mo alloy. (a) SEM-BSE image, (b) SEM-BSE image and EDS mapping and (c) XRD.

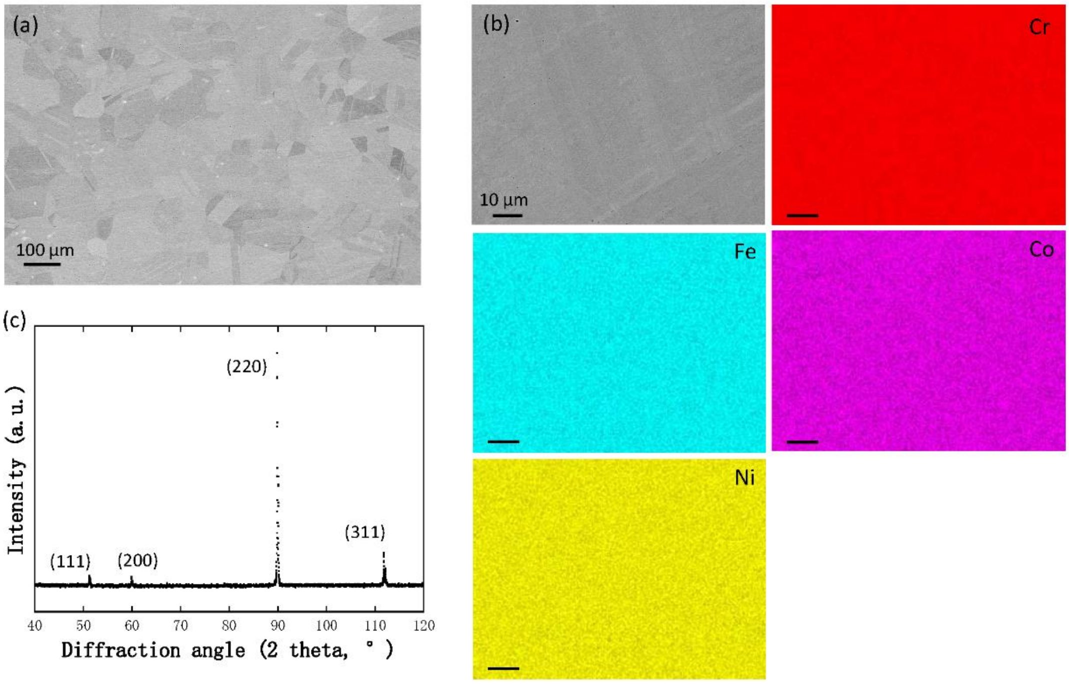

Figure S4 Microstructural characterization of the annealed MPEA-35Cr alloy. (a) SEM-BSE image, (b) SEM-BSE image and EDS mapping and (c) XRD.

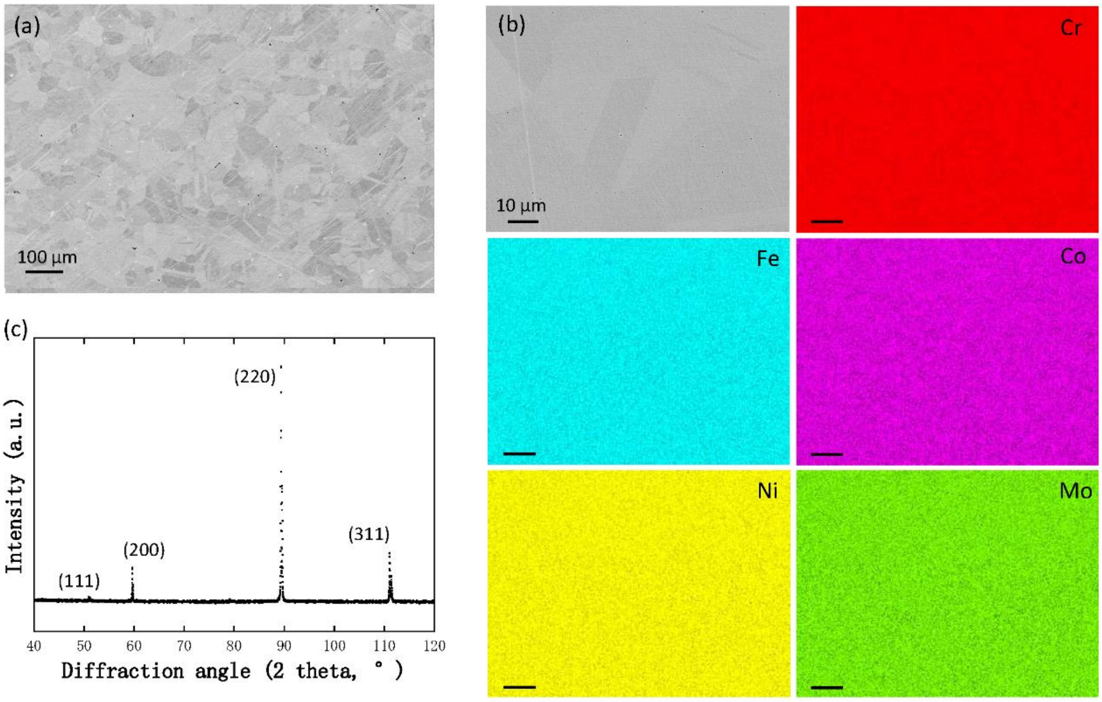

Figure S5 Microstructural characterization of the annealed MPEA-25Cr5Mo alloy. (a) SEM-BSE image, (b) SEM-BSE image and EDS mapping and (c) XRD.